Chapter 6

Joining of monolith SiC ceramic

Ni-based alloys provide good brazing filler characteristics for the many applications of SiC ceramics. Nevertheless, the presence of graphite is unavoidable in the reaction between Ni and SiC, leading to significant degradation of the mechanical properties of the joint. This study investigates the effect of Mo in Ni-30Si alloy on the brazing of SiC at 1300°C, to regulate interfacial reactions and reduce residual stresses by decreasing overall CTE values throughout the brazing process. The addition of Mo up to 8 at.% efficiently suppresses graphite accumulation by converting it into Mo_2C+Ni_3Mo_3C phases, lowering the CTE to 5.4×10^{-6} /°C. When the Mo loading exceeds 12 at.%, the interactions between the filler and SiC are reduced as a result of the non-homogeneous dispersion of Mo. The experimental findings indicate that the joint without graphite has a lap shear strength (LSS) of 107 MPa, which is nearly three times greater than the joint with graphite. Thermodynamic analyses are performed to provide a comprehensive understanding of the underlying mechanisms responsible for the formation of distinct phases in brazed joints.

6.1 Introduction

Silicon Carbide (SiC) ceramics have gained considerable attention as thermo-structural materials for high-temperature applications due to their low density, exceptional specific strength at elevated temperatures, notable resistance to corrosion, and ability to withstand radiation (Snead et al. 2007, Tao et al. 2019). Consequently, SiC finds extensive application across diverse industries such as optical, aerospace, nuclear, automotive, and military sectors (Katoh et al. 2014). Nevertheless, the production of sizable and complex structures poses significant challenges when employing SiC due to its elevated hardness, brittleness, and intricate processing methods (Liu et al. 2022). A more viable approach in this context would

involve the fabrication of SiC components of reduced dimensions, which can afterwards be assembled to form the intended comprehensive integrated structure.

To date, several techniques have been developed to join SiC ceramics (Tatarko et al. 2016, Hernandez et al. 2014). Brazing is a commonly utilised technique for the joining of SiC due to its inherent advantages in terms of simplicity, reliability, and excellent reproducibility (Sciti et al. 2001, Kamal et al. 2023a). A variety of brazing fillers have been developed to facilitate the uniform or varied joining of SiC ceramics. Commercially available Ti- Cu-Ag-based fillers are routinely used due to their exceptional wettability and reactivity with SiC surfaces. Nonetheless, the brazed interfaces suffer from the formation of various brittle compounds, such as TiC, TiCu, Ti_5Si_3, $TiSi_2$, and other intermetallics impairing the overall structural integrity of the joints (Liu et al. 2009, Liu et al. 2014, Moszner et al. 2017, Song et al. 2019a).

Recently Ni-based alloys have been extensively employed in the aviation industry due to their exceptional performance in terms of high-temperature strength, hot corrosion resistance, and machinability (Liu et al. 2013, Long et al. 2018, Song et al. 2019b). Numerous researchers have used Ni-based alloy fillers for joining SiC due to their superior performance at elevated temperatures and resistance to irradiation. Ni-based fillers demonstrate a significant chemical affinity with SiC, resulting in the breaking of the Si-C bond even at relatively low temperatures of 500°C (Kurimoto et al. 2002). The literature presents a comprehensive examination of the reaction mechanism and process involving a Ni-based alloy and SiC (Shi et al. 2020, Shi et al. 2021a).

In certain instances, additional alloying elements, namely Cr, Mo, Cu, Co, and Mn, are intentionally introduced into these alloys to augment their performance in a variety of applications (Liu et al. 2013, Feng et al. 2003, Wang et al. 2020, Wang et al. 2021). Tian et al. studied the bonding process of α-SiC using Ni-Si-Ti fillers and noticed the formation of Ni_3Si_2 and NiSi phases at the interface (Tian et al. 2017). Their findings demonstrated that the presence of Ti promotes the formation of a novel compound, $Ni_{49}Ti_{14}Si_{37}$, within the interlayer region, in addition to the existing Ni-Si compounds (e.g., NiSi and Ni_3Si_2). The joint exhibited a bending strength ranging from 66 to 75 MPa. Nevertheless, there were notable cracks present in the interphase. These cracks can be attributed to the substantial disparity in the coefficient of thermal expansion (CTE) between the Ni-based silicides ($9\text{-}12\times10^{-6}$/°C) and the SiC substrate (3×10^{-6}/°C). To mitigate the residual stresses, Wang et al., designed a brazed filler that consisted of Ni-28Mo, wherein Mo, a low CTE element, was incorporated into Ni (Shi et al. 2021b). According to them, the presence of Mo significantly enhanced the wettability of Ni

on SiC and the joint brazed under the optimum brazing conditions displayed the strengths of 161 ± 27 MPa at 700 ℃. The observed excellent thermal stability can be attributed to the existence of Ni_3Mo_3C and graphite phases. Moreover, they contended that the optimal amount of graphite is crucial in attaining the highest possible performance of the joint. The presence of a low graphite content leads to a uniform distribution of Mo in the interphase, which consequently decreases the level of residual stress whereas, an excessive quantity of graphite adversely affects the structural integrity of the joint. In line with these findings, Shi et al. demonstrated graphite, a prominent by-product in Ni-based fillers, significantly compromises the mechanical properties of β-SiC joints (Shi et al. 2020, Shi et al. 2021a, Shi et al. 2021b, Shi et al. 2022). They found that the inclusion of Zr/Si (up to 40% wt) in the joining fillers has a positive effect, as it eliminates graphite and enhances the mechanical properties of SiC joints. However, due to their pyrophoric nature, Zr powder must be handled and processed with extreme caution (Kullen et al. 1977). Besides, it has been shown that an excessive Zr addition causes difficulties in brazing consolidation due to a massive volume increase, leading to a reduction in joint quality (Chen et al. 2018). In the case of Si-rich filler, the joint strength is promising, but unreacted Si present in braze contributes to facile debonding at the Si-SiC interface at high temperatures, resulting in a joint with poor strength (Singh et al. 1994, Yin et al. 2010). Therefore, to fully harness the potential of Ni-based alloys for bonding SiC ceramics without the formation of graphite and to enhance the processability of Ni-based alloys, it is necessary to incorporate an additional appropriate alloying element.

Considering the comparatively higher melting point (2623ºC) and lower CTE (4.8×10^{-6}/°C) of Mo compared to other alloying elements including Si, Zr, Cr, Cu, Ti, Ag, In, it is worthwhile to investigate the potential applications of Mo. The low CTE exhibited by Mo is anticipated to be advantageous in mitigating the defects generated by thermal residual stress. Moreover, the surplus graphite released by the interaction between Ni and SiC will undergo consumption by Mo, resulting in the formation of advantageous Mo-based carbides that exhibit stability at high temperatures. To the best of our knowledge, no research has been published on the joining of α-SiC ceramics employing a pressureless-brazing technique with a Ni-Si-Mo filler. Therefore, in this study, Ni-30Si alloy powder was mixed with different amounts of pure Mo powders to join SiC ceramics. The microstructure morphologies of the joint and reaction products were examined and analysed using an SEM equipped with an EDS, and XRD. Furthermore, thermodynamic analysis was used in the study to understand the reaction mechanism between the powder filler and SiC. A thorough analysis was performed to examine

the effect of Mo addition on the microscopic structure and mechanical strength of the SiC joint, and lastly, the justification for increasing joint strength is provided.

6.2 Experimental

SiC monoliths were fabricated by the process of hot pressing commercially available α-SiC at temperatures and pressures of 2000 °C and 1500 MPa, respectively. Specimens were cut into a couple of sizes: 10×10×5 mm^3 and 30×10×5 mm^3 using a metal-mounted diamond-based wheel for interfacial microstructural characterisations and LSS evaluation, respectively.

Brazing filler formulations were created using very pure nickel (Ni), silicon (Si), and molybdenum (Mo) powders obtained from M/s. Jagatek Corporation, Hyderabad. The average particle size of Ni, Si, and Mo powders was determined using the Fisher subsieve sizer to be 2.1, 5.3, and 3.5 μm, respectively. It has been shown that the addition of Ni with Si ≤ 30 at.% exhibits excellent reactive wetting behaviour over SiC substrate. Furthermore, increasing Ni content in Ni-Si filler enhances the formation of high-temperature stable Ni-rich phases including Ni_2Si, and Ni_3Si_2 (Kamal et al. 2023b). Therefore, the eutectic composition selected for the brazing material was Ni-30Si, assuring a maximum Si content of 30 at.%. A filler material consisting of Ni-30Si alloy was used in this study, with different amounts of Mo (0, 4, 8, and 12 at.% or 0, 7.6, 14.5, and 20.9 wt.%). These filler compositions were labelled as Mo-0, Mo-4, Mo-8, and Mo-12, respectively, and were employed for the brazing process of SiC. With the aid of isopropyl alcohol (IPA) as a dispersing medium, the filler components were mixed in an agate pot. The mixture was then blended in a planetary ball mill for 4 h duration followed by the removal of IPA at 80°C in an inert environment.

Surface preparation of the SiC specimens was carried out using 320 SiC grit paper. Before conducting the brazing experiment, an ultrasonic cleaning procedure was performed for 15 min, followed by a drying process at 150°C. To enhance the adherence of the filler to the substrate, a paste was prepared by mixing it with acetone. This paste was then placed onto both connecting surfaces of SiC using a nylon brush. Multiple applications of the coating were made until the final ~100 μm of coat thickness was achieved. Physical measurements were taken with a digital vernier calliper to determine the thickness of the coating. The coated surfaces were then dried in an ambient environment for 30 min before loading for the brazing experiment. Following this, the specimens were placed into a high vacuum brazing furnace with minimal dead load applied to provide adequate interaction between bonding surfaces. The bonding experiment was performed at a temperature of 1300±10°C, with a controlled heating/cooling

cycle. The experimental conditions encompassed a heating/cooling rate of 5°C/min, a soaking period of 30 min, and a vacuum pressure of 10^{-3} mbar. The SiC ceramic bonds were labelled as J-Mo-0, J-Mo-4, J-Mo-8, and J-Mo-12, corresponding to the filler formulations Mo-0, Mo-4, Mo-8, and Mo-12, respectively.

The experimental procedure involved doing a differential scanning calorimetry (DSC) test under the conditions of a ramp of 10°C/min within an argon atmosphere. The average particle size of all elemental powders was measured using a subsieve auto-sizer (ASTM B330).

A wetting test was conducted on all four types of fillers on a SiC substrate using the brazing conditions specified above, as outlined for SiC bonding. The contact angle of droplets was analysed using an optical microscope (Brand: Olympus). All of the filler formulations were heated at 1300°C for 30 min before pelletizing to a size of 5 mm×5 mm×10 mm. Following that, CTE was evaluated using a thermo-mechanical analyser (Brand: TA Instruments TMA Q400) between 25 and 800°C following ASTM E-831. The maximum standard deviation in CTE values was observed to be $\pm 0.5\times10^{-6}$/°C.

The mechanical strength of the joint was assessed by evaluating lap shear strength (LSS) as per the procedures mentioned in our previous work (Kamal et al. 2023b). The LSS test was conducted until the joint experienced total fracture, with 0.5 mm/min cross-head speed. For all types of joining, three sets of specimens were tested, and the average value was used for reporting purposes.

The samples were mounted in transparent epoxy upto a temperature of 140°C. Hot press epoxy mounted samples were polished to 1 μm grit finish using Carbimet cloth, Texmet C cloth, micro-cloth, micro-polishing suspension, and alumina suspension to investigate the microstructure of the joint interface using a field emission scanning electron microscope (FE-SEM) (Brand: Zeiss Supra 55) by employing the accelerating voltage up to 15 kV. The atomic composition of elements present was estimated by an energy dispersive spectrometer (EDS) (Brand: Bruker X Flash 6160) with a counting duration of 60 s.

The phases were identified using XRD (Brand: Philips) by impinging an X-ray beam at the specimen through Cu-Kα radiation (λ : 1.5418 Å, step size: 0.02°, time per step: 0.5 s) at 25° C. The present filler system was analysed using EDS and XRD techniques, resulting in the identification of two binary phase diagrams (Ni-Si and Mo-C) and two ternary phase diagrams (Ni-Si-C and Ni-Mo-C). These binary and ternary phase diagrams are depicted in Fig. 6.5 and 6.7. Consequently, the thermodynamic calculations were performed utilising the Thermo-calc® programme package.

6.3 Results and Discussion

6.3.1 Brazing Filler Characterisation

The melting range of the fillers is determined using DSC testing, which is performed at temperatures of up to 1400°C. The results exhibit the noteworthy energy change in two distinct temperature regimes i.e., 950-1030ºC and 1230-1280°C as illustrated in Fig. 6.1. The exothermic peaks in the 950-1030ºC temperature range are assigned to the interaction of Ni and Si to form Ni-Si-based compounds (e.g., NiSi, Ni_3Si_2) and concurrent grain growth (Tian et al. 2017). The presence of an endothermic energy peak in the second region indicates that the filler material starts to melt at temperatures higher than 1230°C and completes melting at about 1280°C. To guarantee sufficient melting, a temperature slightly over the upper threshold of 1280°C, specifically 1300°C, was chosen for the brazing experiment. Therefore, a total of four types of joints were prepared and subsequently subjected to further microstructural and mechanical characterizations.

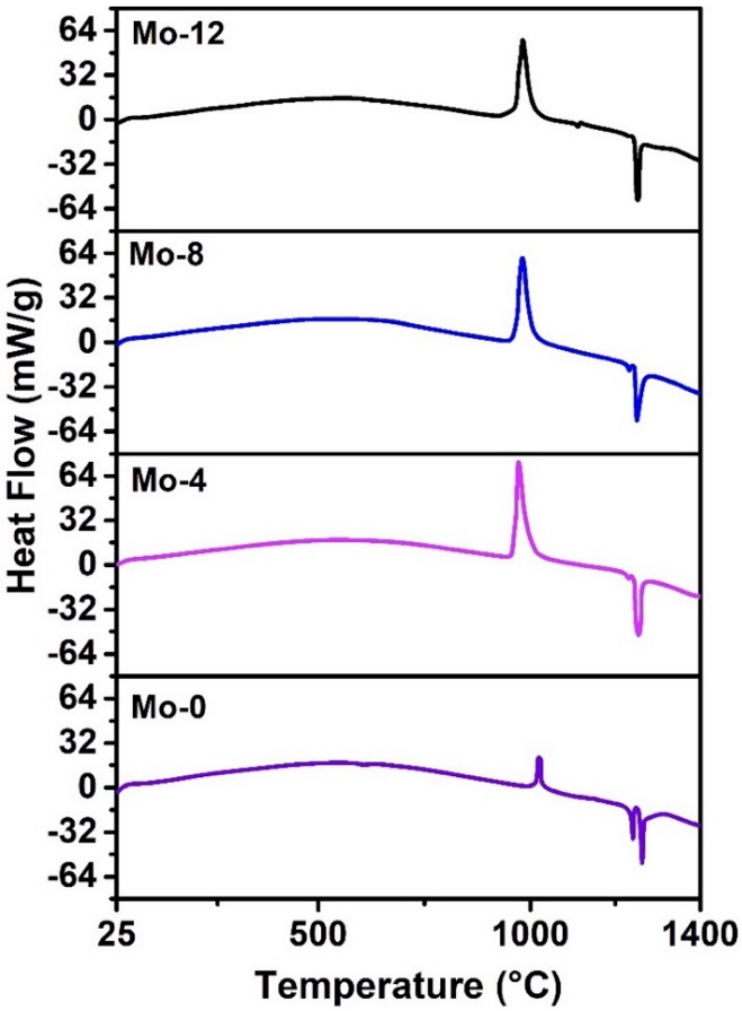

Fig. 6.1: DSC curves of various brazing fillers.

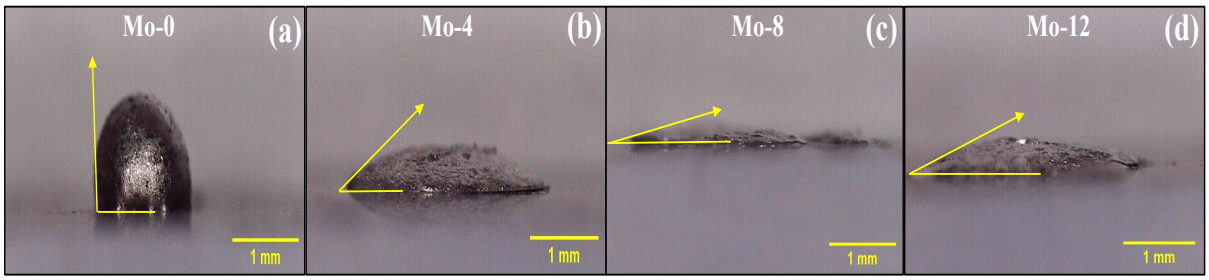

Fig. 6.2: Wettability study of (a) Mo-0, (b) Mo-4, (c) Mo-8, and (d) Mo-12 fillers on SiC at 1300ºC.

The wettability study was carried out to assess the spreading characteristics of the brazing fillers over α-SiC ceramic substrate at 1300°C. It is to be noted that α-SiC now onward will be denoted as SiC throughout the text for convenience. The wettability test utilised for determining the contact angle is depicted in Fig. 6.2. The contact angle measured for Mo-0 was as high as 93±3°, indicating its unsuitability for the brazing operation. According to the literature, the inclusion of wettable particles dramatically affects the rheological properties of the blend, causing the viscosity to noticeably reduce as a result of a decrease in the surface energy of melt (Xu et al. 2013, Zhang et al. 2014, Fathian et al. 2017). The addition of Mo contributed to a significant decrease in the contact angle to 38±3° for the Mo-4 sample and 14±2° for the Mo-8 sample. Interestingly, Mo loading above 8% increased the contact angle to 22±2° (Mo-12). This might be because of the substantial creation of the Mo-based hard carbides, which impede flow and are detailed in the following section. In summary, the low wettability of the braze filler formulation without Mo makes it unsuitable for the joining of SiC and all the Mo-based fillers satisfactorily wetted the surface of SiC, indicating to act as a potential material for the brazing.

6.3.2 Microstructural characterisation of joints

Microstructure, line scans, and EDS map for the cross-sectional interface of J-Mo-0, as captured by SEM-EDS, are presented in Fig. 6.3. It is obvious that the interface is abundant in voids and cracks. Before the brazing, the interphase exhibited a thickness of 100 µm. However, as a result of adequate melting, enhanced flowability, and the oozing out of liquid braze from the edges, this thickness is subsequently decreased to ~43 µm. The interface is categorised into two zones namely zone-A and zone-B (see Fig. 6.3a). Zone-A is a continuous reaction region of thickness ~17 µm located at the centre of the braze while a relatively thinner zone-B namely interfacial reaction zone (IRZ) of ~13 µm, is created at the conforming surfaces of braze and substrate on either side. According to the line scan (Fig. 6.3b) and elemental map (Fig. 6.3c),

zone-A has Ni and Si or Ni-Si-based compounds (e.g. Ni_2Si, Ni_3Si_2) that are uniformly distributed, whereas zone-B is an IRZ that contains Ni-Si-based compounds and graphite clusters. A fraction of the Ni rapidly diffused away from the centre, reacting with the SiC to form Ni-Si-based compounds, and releasing graphite which then aggregated at IRZ forming clusters, as shown in Fig. 6.3c (Shi et al. 2020). It is evident that these clusters are connected with narrow bridges passing through the grey-coloured islands.

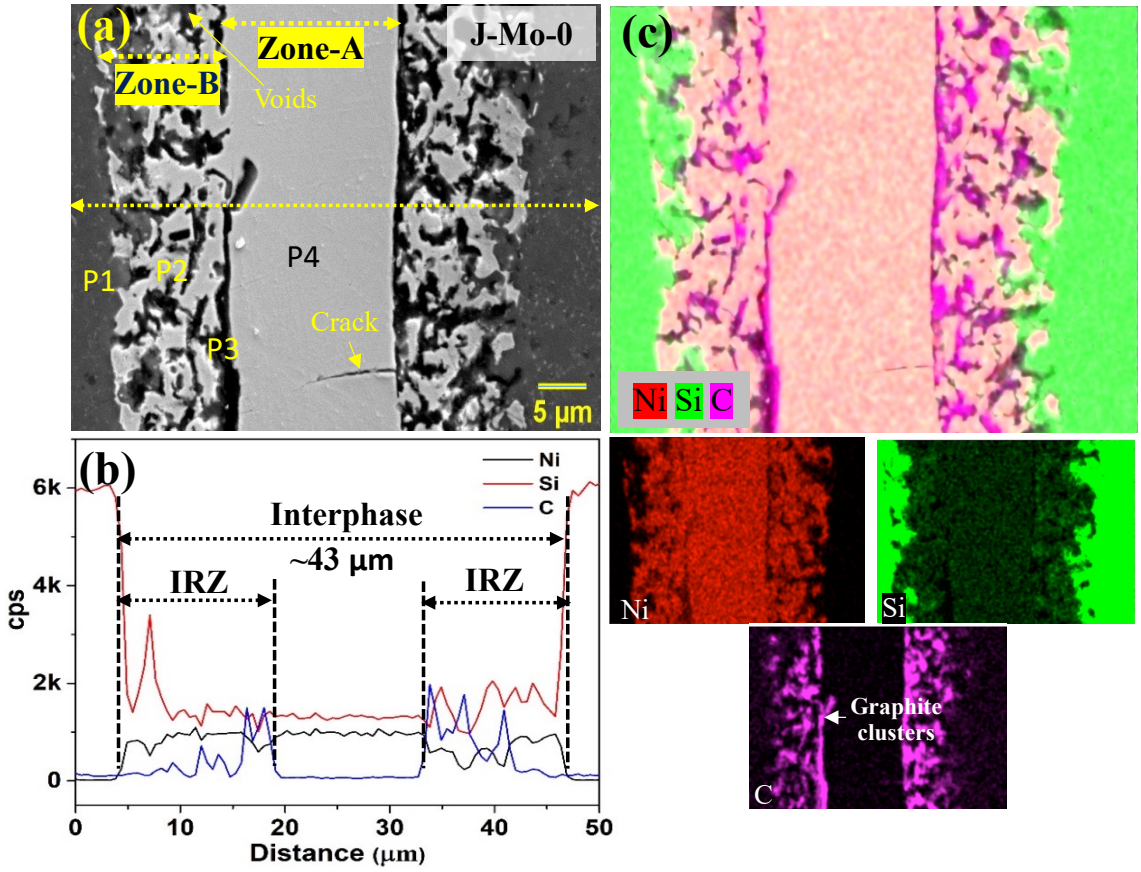

Fig. 6.3: (a) SEM image, (b) line scans, and (c) EDS mapping of J-Mo-0.

As suggested by the EDS map (Fig. 6.3c), the grey colour islands are mainly Ni-Si-based compounds, which seem elongated polygonal grains embedded in graphite clusters. The IRZ resembling a dendritic structure is formed on both sides of the braze due to a vigorous interaction between Ni and SiC according to reactions (6.1) and (6.2) resulting in precipitation of graphite. The cracks or crevices that occurred at the interface are attributed to the large differences in CTE between Ni-Si-based compounds (13.6×10^{-6}/°C), graphite ($1.5\text{-}2\times10^{-6}$/°C), and SiC ($3\times10^{-6}$/°C), which led to a high concentration of residual stresses during the cooling

process. EDS point analysis is used to determine the elemental composition of the various phases, which were recognised as points P1 to P4 in SEM images.

Table 6.1: Elemental composition and primary phases for all SiC-SiC joints

Sample	Point	Composition (at. %)				Major phases
		Ni	Si	C	Mo	
J-Mo-0	P1	0.9	55.6	43.5	--	α-SiC
	P2	58.5	30.9	10.6	--	δ-Ni_2Si+Ni_3Si_2
	P3	1.5	1.8	96.7	--	graphite
	P4	59.4	29	11.6	--	δ-Ni_2Si
J-Mo-4	P5	0.8	53.0	45.0	0.2	α-SiC
	P6	53.5	28	18.1	0.4	δ-Ni_2Si+Ni_3Si_2
	P7	18.2	8.1	23.2	50.5	Mo_2C
	P8	61.1	29.2	8.9	0.8	δ-Ni_2Si
J-Mo-8	P9	0.2	52.8	46.6	0.4	α-SiC
	P10	53.2	27.9	18.5	0.4	δ-Ni_2Si + Ni_3Si_2
	P11	18.9	7.8	24	49.3	Mo_2C
	P12	61.6	32.1	5.7	0.6	δ-Ni_2Si + Ni_3Si_2
J-Mo-12	P13	0.7	45.6	53.2	0.5	α-SiC
	P14	52.9	28.3	18.6	0.2	δ-Ni_2Si+Ni_3Si_2
	P15	1.5	1.8	96.2	0.5	graphite
	P16	50.5	5.1	5.0	39.4	Ni_3Mo_3C
	P17	57.1	39	3.5	0.4	Ni_3Si_2

The atomic composition of all elements detected and corresponding possible predominant phases are presented in Table 6.1. The elemental composition measured at P1 indicates that it corresponds to the SiC substrate. Point P2 (grey colour) is rich in Ni and the atomic composition indicates δ-Ni_2Si and Ni_3Si_2 phases formed while P3 (black colour) is mainly graphite clusters released by the reaction of Ni and SiC according to reactions (6.1) and (6.2). It appears that the atomic composition at P4 is broadly suggestive of a freshly generated δ-Ni_2Si phase as per reactions (6.3) and (6.4). According to the elemental distribution, the majority of the Ni from the braze filler reacts with Si and forms the core zone (zone-A), while the remaining Ni diffuses towards SiC to contribute to the Ni-SiC interaction at the interface.

It is worth mentioning that a small amount of Ni is present in the SiC phase at P1, likewise, the presence of C in the Ni-Si phase at P2 and P4 is also very meagre. This observation demonstrates that the solubility of C in Ni-Si alloys and Ni in SiC is significantly low, consistent with previous research findings (Shi et al. 2020).

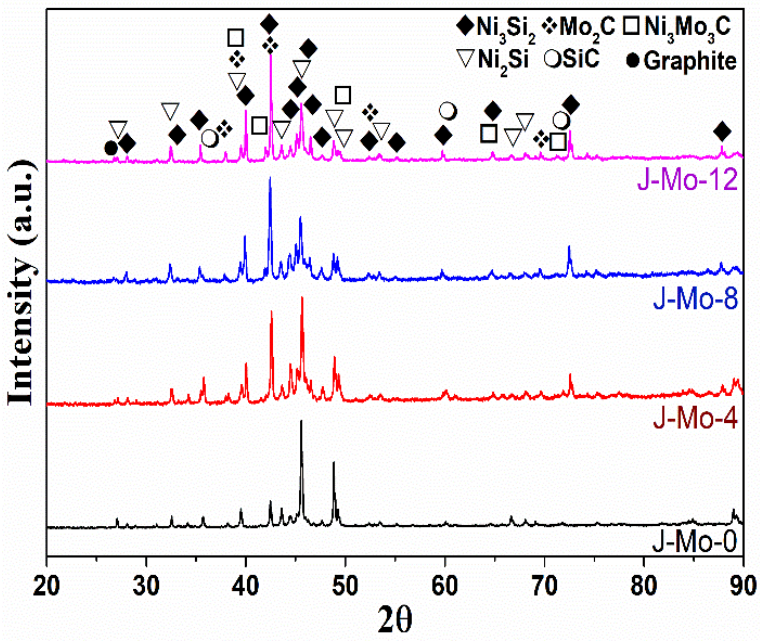

Fig. 6.4: XRD pattern for the interface of SiC-SiC joints.

The XRD pattern of J-Mo-0, as depicted in Fig. 6.4, provides additional support for the presence of newly formed phases, including δ-Ni_2Si, Ni_3Si_2, and graphite. To provide further theoretical validation of the possible production of phases, thermodynamic calculations were conducted using the Thermo-calc® program. Fig. 6.5 presents the Ni-Si binary and Ni-Si-C ternary phase diagram, whereby it is observed that there is no tie line connecting Ni and SiC. This absence of a tie line signifies that these phases are not in thermodynamic equilibrium implying that the solubility of Ni in SiC is considerably limited. Consequently, it is plausible to infer from the EDS analysis that a reaction between Ni and SiC can occur, as shown by reactions (6.1) and (6.2) (see Table 6.1). Moreover, the phase diagram exhibits multiple equilibrium domains, notably the liquid+δ-Ni_2Si+graphite domain shown by a blue triangle, the liquid+θ-Ni_2Si+graphite domain represented by a green triangle, and the liquid+graphite domain represented by a magenta triangle. Therefore, the formation of δ-Ni_2Si, θ-Ni_2Si, and graphite is thermodynamically possible at 1300ºC. The phase domain associated with the atomic composition of P2 and P4 composition provides evidence that the phases δ-Ni_2Si/θ-Ni_2Si, graphite, and liquid are in equilibrium. It is noteworthy that the θ-Ni_2Si phase is not

observed in our investigation and the formation of the Ni_3Si_2 phase is suggested by XRD analysis. It is unlikely that Ni_3Si_2 will be found at the joining interface, as shown by the Ni-Si-C phase diagram (Fig. 6.5b). According to earlier research, the creation of Ni_3Si_2 in this context can be attributed to the eutectoid transition of θ-Ni_2Si into δ-Ni_2Si and Ni_3Si_2 while cooling the joint. Consequently, the XRD analysis does not reveal the presence of θ-Ni_2Si, a metastable compound that remains unstable at ambient temperature (Shi et al. 2020). In summary, the Ni-30Si alloy demonstrated successful brazing of SiC ceramics. However, it encountered challenges such as excessive graphite precipitation, replete with defects, and the development of IRZ. The joining interface witnessed a vigorous reaction of Ni with SiC producing δ-Ni_2Si, Ni_3Si_2, and graphite phases. The presence of graphite and δ-Ni_2Si +Ni_3Si_2 is mostly observed in the IRZ, while the central zone exhibited a dominant phase of δ-Ni_2Si.

R1: $2Ni + SiC \rightarrow Ni_2Si + C$ ΔG = -101 kJ/mol (6.1)

R2: $3Ni + 2SiC \rightarrow Ni_3Si_2 + 2C$ ΔG = -94 kJ/mol (6.2)

R3: $Ni + Si \rightarrow NiSi$ ΔG = -114 kJ/mol (6.3)

R4: $Ni + NiSi \rightarrow Ni_2Si$ ΔG = -124 kJ/mol (6.4)

R5: $Ni_2Si + NiSi \rightarrow Ni_3Si_2$ ΔG = -119 kJ/mol (6.5)

R6: $2Mo + C \rightarrow Mo_2C$ ΔG = -58 kJ/mol (6.6)

R7: $3Ni + Mo + Mo_2C \rightarrow Ni_3Mo_3C$ ΔG = -38 kJ/mol (6.7)

Fig. 6.6 shows the microstructure, line scans, and EDS mapping of the joint interface of J-Mo-4. The interphase evolved into a more homogenous and continuous structure and narrowed to ~26 μm thickness. The incorporation of 4% Mo into the Ni-30Si filler led to a significant reduction in defects, except for a limited number of cracks and voids observed in the braze, as evident in Fig. 6.6a. The interphase is mostly constituted of two morphologies: grey matrix (zone-A) and white flocculants (zone-B). In the interphase, zone-A is the bulk phase, wherein zone-B is sparsely distributed within the former. Line scans (Fig. 6.6b) and elemental map (Fig. 6.6c) indicate that zone-A is mainly Ni-Si-based compounds (e.g. Ni_2Si, Ni_3Si_2) and zone-B is Ni-Mo-C-based compounds (e.g. Mo_2C, Ni_3Mo_3C). According to the EDS point analysis (Table 6.1), it can be observed that point P5 corresponds to the SiC substrate, similar to J-Mo-0. P6 (near to interface) and P8 (at the centre of the braze) are Ni-

rich phases. The atomic compositions at P6 and P8 suggest the presence of δ-Ni_2Si+Ni_3Si_2, and δ-Ni_2Si phases with some amount of graphite, respectively.

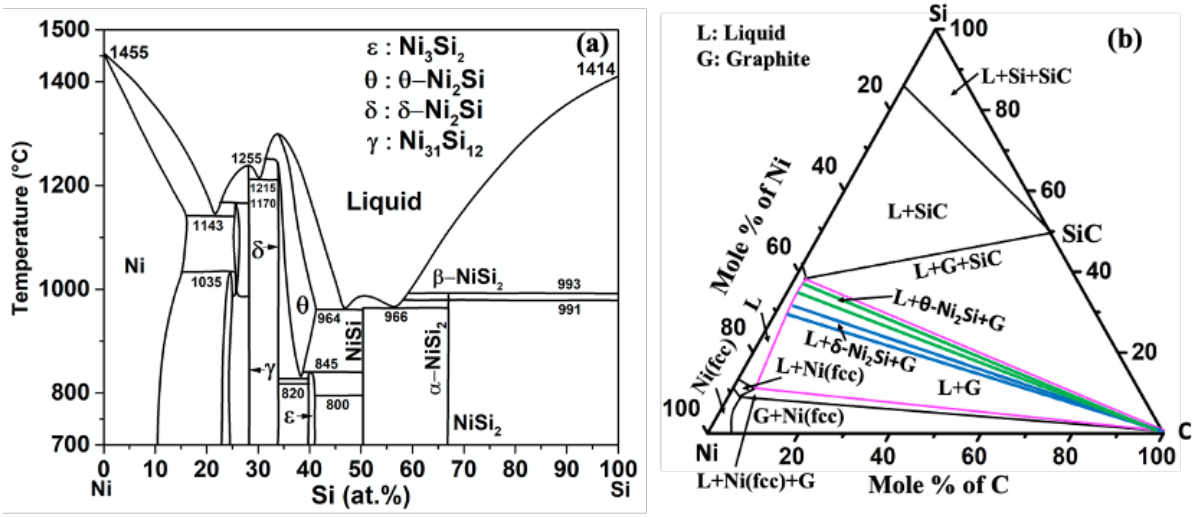

Fig. 6.5: (a) Ni-Si binary, and (b) Ni-Si-C ternary phase diagram at 1300ºC.

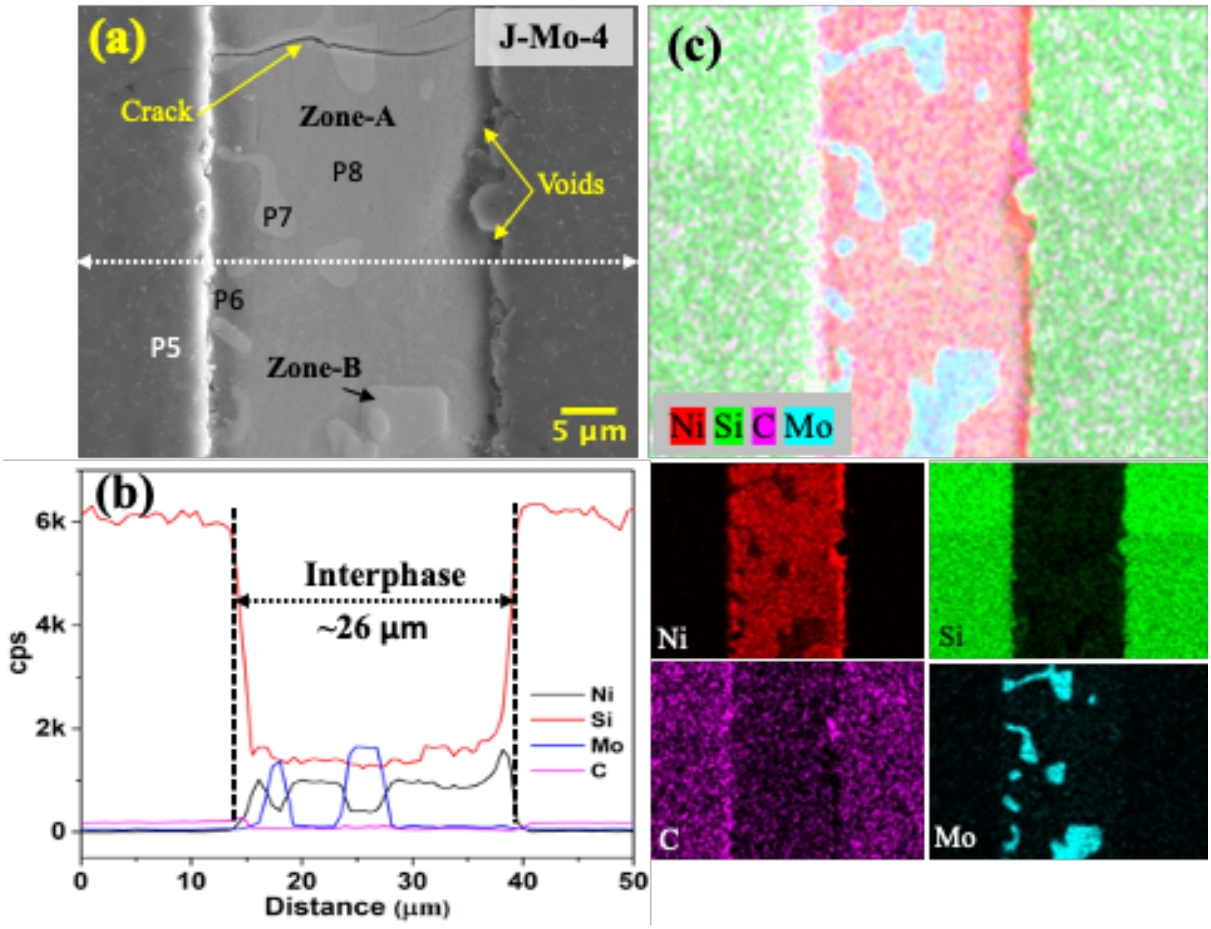

Fig. 6.6: (a) SEM image, (b) line scans, and (c) EDS mapping of J-Mo-4.

As discussed earlier, the formation of δ-Ni_2Si, Ni_3Si_2 is thermodynamically possible and these phases are in equilibrium with graphite, as depicted in Fig. 6.5. Hence, the appearance

of δ-Ni_2Si, Ni_3Si_2, and graphite as newly identified phases following reactions (6.1)-(6.5) is in agreement with the observations made using EDS and XRD techniques. The elemental analysis at P7 in the Mo-rich (zone-B) reveals the presence of Mo_2C, along with a tiny quantity of Ni_3Mo_3C as indicated by reactions (6.6) and (6.7). This finding is further supported by the XRD shown in Fig. 6.4. The formation of Mo_2C and Ni_3Mo_3C is thermodynamically feasible according to Mo-C and Ni-Mo-C phase diagrams, as illustrated in Fig. 6.7 (Regmi et al. 2014, Wang et al. 2021).

It is noteworthy to mention that the Mo-inclusion helped alleviate crack formation by reducing the overall CTE of the filler from 13.6×10^{-6}/°C to 6×10^{-6}/°C. Moreover, the graphite that was released by reactions (6.1) and (6.2) is utilised by Mo to form Mo_2C as described in reaction (6.6). Consequently, the newly formed Mo_2C then reacted with the locally present Ni to yield Ni_3Mo_3C as shown in reaction (6.7). In contrast to the findings of J-Mo-0, the presence of a delineated graphite zone is not observed. The absence of a graphite zone is advantageous for joint strength, as the former reduces the physical strength of a joint owing to poor bonding characteristics (Song et al. 2014, Shi et al. 2021b). In addition, the interaction between graphite and Mo resulting in the formation of Mo_2C, as well as the limited diffusion of Ni caused by its conversion into Ni_3Mo_3C by Mo_2C, played a pivotal role in inhibiting the development of an IRZ. The aforementioned hypothesis is additionally corroborated by the thermodynamic calculation presented in the Ni-Si (Fig. 6.5a), Mo-C (Fig. 6.7a), and Ni-Mo-C (Fig. 6.7b) phase diagrams, which confirm the feasibility of the formation of δ-Ni_2Si, Ni_3Si_2, Mo_2C, Ni_3Mo_3C, and graphite phases. The aforementioned compounds exhibit high melting points and remarkable corrosion resistance (Wang et al. 2021).

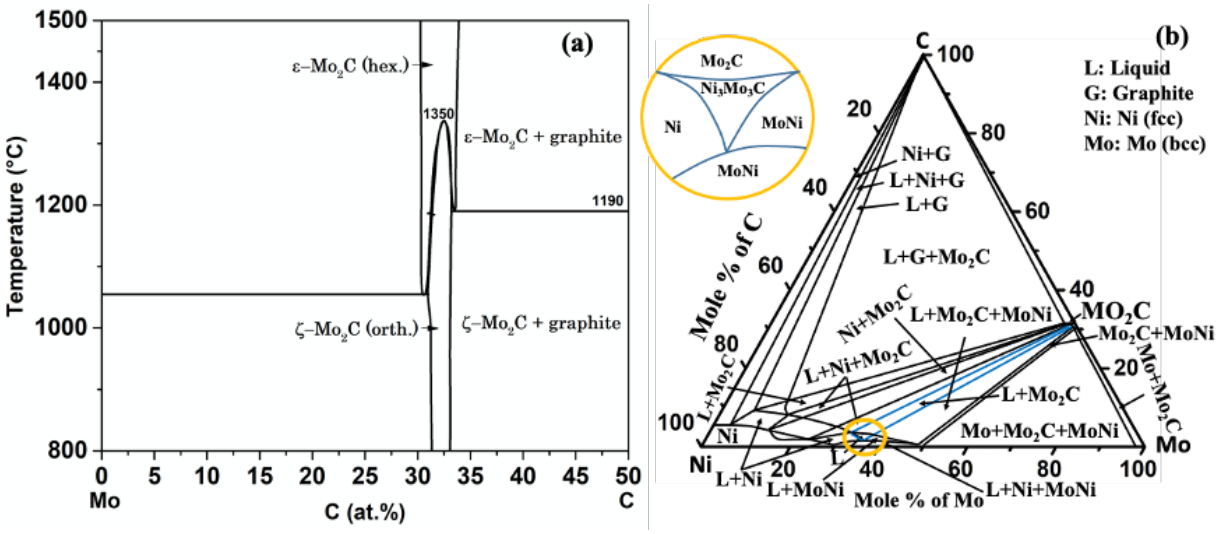

Fig. 6.7: (a) Mo-C binary, and (b) Ni-Mo-C ternary phase diagram at 1300ºC.

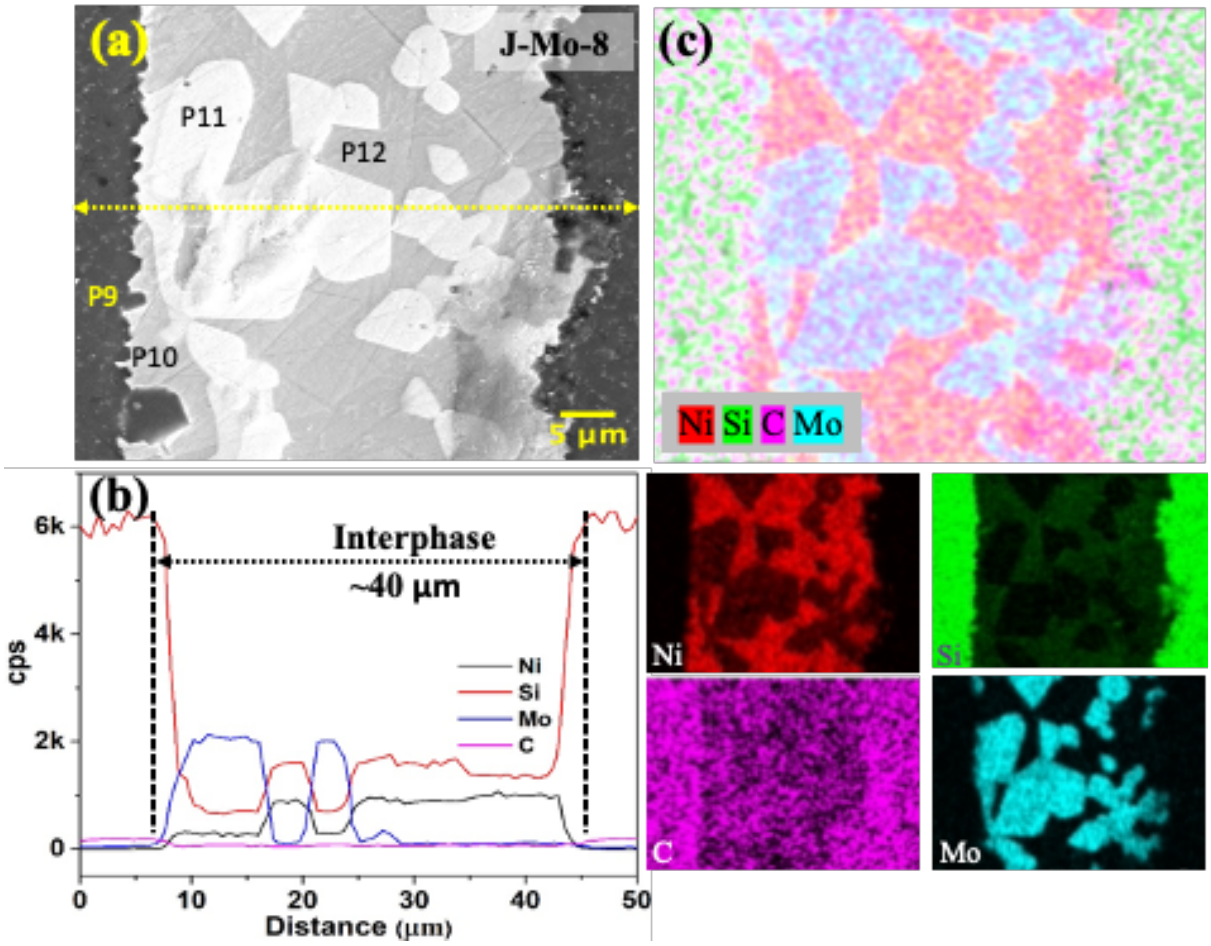

Fig. 6.8: (a) SEM image, (b) line scans, and (c) EDS mapping of J-Mo-8.

Based on previous discussions, it can be concluded that incorporating a 4% Mo content into the Ni-30Si filler resulted in a significant reduction in the occurrence of defects. Nevertheless, it is crucial to acknowledge that the joint has several imperfections. In light of this, the concentration of Mo is increased to 8% and the joint interface of J-Mo-8 is depicted in Fig. 6.8. The SEM micrographs reveal the creation of a joint, which was devoid of any defects such as cracks, crevices or voids. The absence of defects could be due to the integration of low CTE Mo into the Ni-30Si filler. As a result, the CTE value was lowered to 5.4×10^{-6}/°C, a 60% drop when compared to Mo-0. This reduction successfully mitigated the thermal stress experienced during the cooling process. The interphase thickness slightly increased to ~ 40 µm, and can be divided mainly into two regions i.e., grey matrix (zone-A) and white flocculants (zone-B), similar to J-Mo-4. The white flocculants are observed to be evenly distributed within the grey matrix in the braze. EDS line scan and map analyses (Fig. 6.8b and 6.8c) reveal that white flocculants are in the Mo-rich phase while the grey phase is predominantly composed of Ni. Additionally, in comparison to J-Mo-4, there is a notable increase in the overall area encompassed by white flocculants, which rose from 160 to 645 µm^2 (calculated by image

analysis). Similar to earlier instances, EDS point analysis at P9 reveals that it is the SiC substrate itself. The grey region at P10 (near interface) and P12 (centre of the braze) predominantly comprise Ni. The absence of Mo suggests the existence of δ-Ni_2Si and Ni_3Si_2 phases in these regions. The atomic composition of the white flocculant (P11) confirmed the production of Mo_2C with some amount of Ni_3Mo_3C. The newly formed phases viz., δ-Ni_2Si, Ni_3Si_2, Mo_2C, and Ni_3Mo_3C as indicated by EDS analysis were further confirmed by the XRD result (Fig. 6.4). To this end, 8 % Mo addition to Ni-30Si filler rendered a defect-free joint with the formation of high-temperature and corrosion-resistant new phases. Further, Mo_2C with some amount of Ni_3Mo_3C phases appeared as a white flocculant, which is homogeneously distributed in the grey matrix comprising δ-Ni_2Si+ Ni_3Si_2.

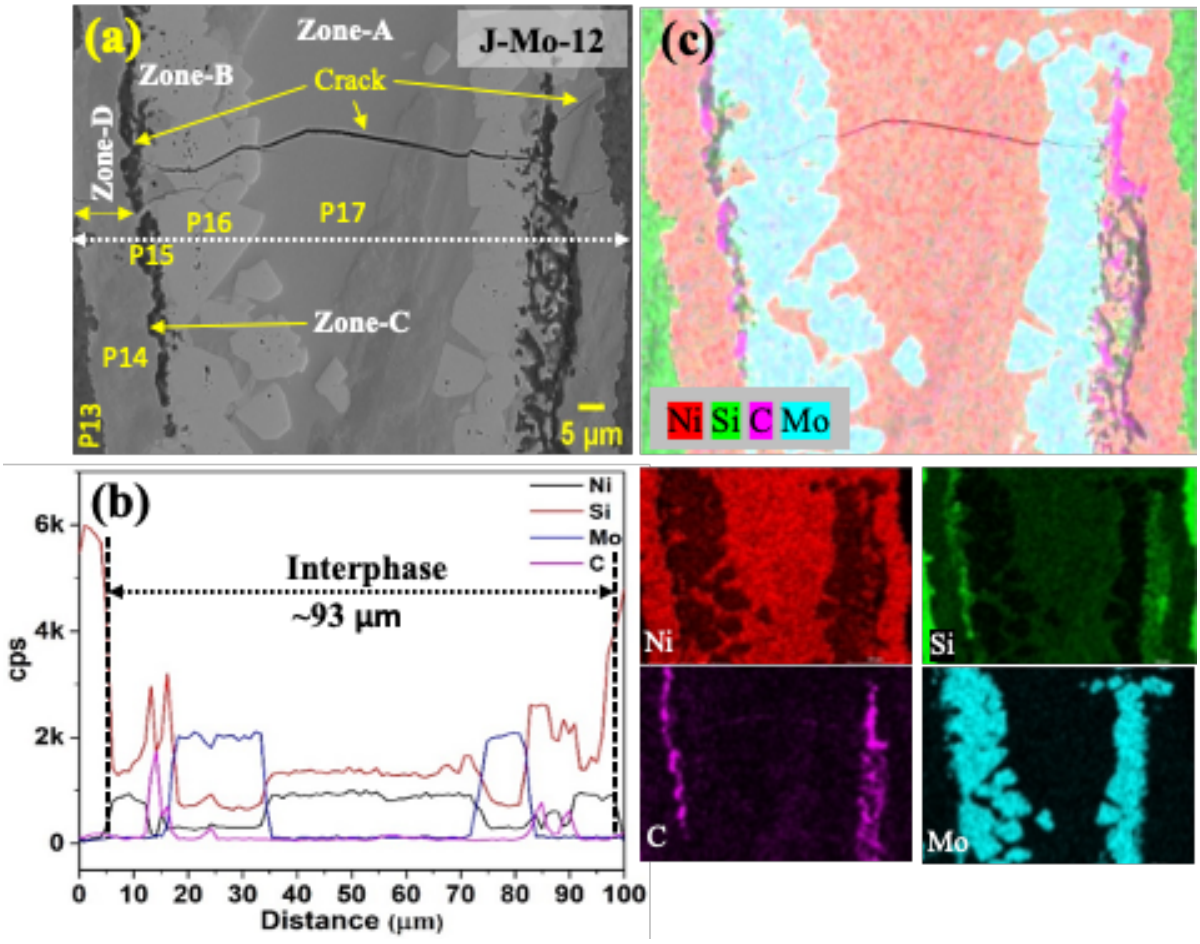

Fig. 6.9: (a) SEM image, (b) line scans, and (c) EDS mapping of J-Mo-12.

To investigate the potential consequences of augmenting the Mo loading in the Ni-30Si filler, the Mo content increased to 12%. The SEM micrographs, line scans, and EDS map of the joint prepared with 12% Mo-based braze alloy (J-Mo-12) are presented in Fig. 6.9. It is noteworthy that the interphase exhibits a thickness greater than twice that of the J-Mo-4 (~26

μm) and J-Mo-8 (~40 μm) joints, measuring ~93 μm. Furthermore, the interphase may be subdivided into four distinct zones, namely A, B, C, and D. Grey colour zone-A (~40 μm) at the centre of the joint is homogenous and continuous, whereas zone B (~23 μm on either side) is white in colour.

In contrast to previous instances, the white-coloured region (referred to as zone-B) exhibits a vertically continuous layer positioned along the interface connecting zone-A and zone-C. The zone-C denotes a relatively thin stratum, ~2 μm in thickness, which formed in the intermediate region between zone-B and D. The zone-D grey in colour, located close to the SiC substrate, is characterised by a vertically aligned layered structure with a thickness of ~13 μm.

Line scans (Fig. 6.9b) and EDS map (Fig. 6.9c) demonstrate that zone-A and -D are homogeneous and primarily consist of Ni-Si-based compounds. The elemental composition of zone B, on the other hand, supports the presence of Ni-Mo-C-based compounds. Zone-C refers to a lamellate graphite layer structure that is sandwiched between zone-B and -D. As previously stated, the Ni-containing liquid filler diffuses towards SiC, leading to a reaction that releases C atoms. In general, C atoms have low solubility and diffusivity in Ni-Si-based compounds and SiC ceramics (Cao et al. 2006). As a result, the C atoms precipitate out, forming a distinct graphite layer that provides a steady supply to the Mo-rich phase. Concurrently, on the braze side, Mo concentration is extremely high and forms a continuous zone due to their aggregation along the interface. This zone acts as a barrier to the Ni/Mo diffusion from the centre of the braze towards SiC. Consequently, the lamellated graphite structure (zone-C) is generated along with the Ni-rich (zone-A) and Mo-rich (zone-B) phases. The composition analysis at P13 confirms the presence of a SiC substrate (see Table 6.1), consistent with previous observations. The atomic concentration at P14 (zone-D) indicates the presence of δ-Ni_2Si, Ni_3Si_2, and graphite produced according to reactions (6.1) and (6.2). The graphite layer (P15) precipitated, aggregated, and developed as a distinct zone-C at the interface of zone-B and -D as explained above. The presence of a thick white layer (P15 at zone B) indicates the existence of a Mo-rich phase consisting of Ni_3Mo_3C. The area occupied by Mo-rich phases increased up to 2567 μm^2 in comparison to J-Mo-4, which can be attributed to the excessive loading of Mo. The P16 located in zone-A is associated with the formation of the Ni_3Si_2 phase. This finding is consistent with the higher peak intensity seen for J-Mo-12 in the XRD analysis (see Fig. 6.4). Thus, the phases suggested by EDS are consistent with XRD analysis and thermodynamic calculations as explained for earlier cases. Despite the observed drop in the CTE of the Mo-12 filler to 5.1×10^{-6}/°C, the formation of cracks still occurred due to the growth of different phases within

the interface. The presence of both transverse and longitudinal cracks in the contact is evident in the SEM image (Fig. 6.9a). The presence of a longitudinal crack can be ascribed to the thermal mismatch that occurs between the Ni-rich (zone-D), graphite (zone-C), and Mo-rich (zone-B) phases during the cooling process, resulting in the accumulation of significant residual stress. The considerable thickness of the braze renders it vulnerable to cracking, resulting in the transverse propagation of a longitudinal crack during the cooling phase. In the end, the incorporation of 8% Mo into a Ni-30Si alloy resulted in the formation of a joint without any defects, exhibiting a consistent microstructure at the interface. The distribution of Ni-rich and Mo-rich regions is homogeneous across the interface, with no evidence of defects, IRZ or unreacted graphite.

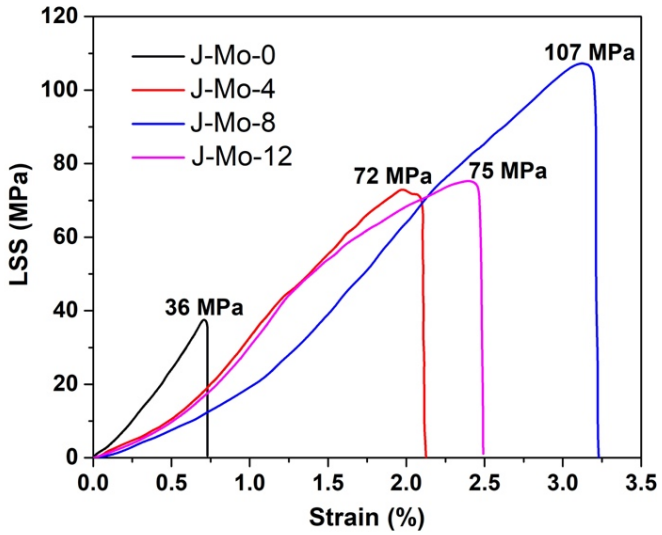

Fig. 6.10: LSS stress-strain graph of SiC-SiC joints.

6.3.3 Mechanical performance of joints

The SiC joints were evaluated for single offset LSS using different Mo-containing Ni-30Si alloys, and the corresponding LSS stress-strain curves are presented in Fig. 6.10. SEM-EDS was used to characterise the fractured surface of the joints (Fig. 6.11) to gain a better understanding of the morphology and composition at the de-bonded sites. The joint without Mo (J-Mo-0) failed at an LSS of 36 MPa with a maximum displacement of 0.74%. This is owing to the presence of multiple voids, cracks, and fissures caused by a large difference in CTE between the filler material and the SiC substrate. Moreover, the insufficient wettability of the filler hindered the adequate spreading and penetration in the joining interfaces, resulting in a deficiency of adhesion. Additionally, the presence of a crack (see Fig. 6.11a) and a significant quantity of graphite phase (Fig. 6.11b), resulting from the reaction between Ni and SiC, are the contributing factors to the reduced strength of the joint. This is caused by the coarsening and

detachment of the graphite phase from the Ni-Si phases, which occurs due to the accumulation of stresses (Shi et al. 2020).

The incorporation of a 4% Mo content as a stress-relieving agent resulted in a twofold increase in the LSS value, reaching 72 MPa for the J-Mo-4 joint. This exhibits that the addition of Mo has a noticeable influence on the microstructure, wettability, adhesion, and infiltration characteristics of the Mo-4 braze alloy as discussed in the previous section. The fracture occurred at the SiC substrate, as seen in Fig. 6.11c and 6.11d, confirms that Mo devoured the majority of the graphite, and the presence of voids near the SiC substrate acted as the weakest point for the onset and propagation of cracks during testing. By including a higher quantity of Mo, the LSS experienced a subsequent increase to 107 MPa with a higher strain value, representing a significant 197% improvement compared to the J-Mo-0 joint. Mo refines the microstructure and strengthens the Ni-based silicide matrix by forming Mo-based carbide phases. When a load is applied, sliding the heterogeneous phase boundaries facilitates plastic deformation before fracture, resulting in increased strain with improved bond strength (Manikandan et al. 2019, Guo et al. 2020, Vedela et al. 2021). The dense microstructure at the interface in Fig. 6.11e confirms that the fracture took place at the interlayer, which was made up of Ni-rich and Mo-rich phases (Fig. 6.11f). Furthermore, there are no crack or graphite phases at the fracture site. Therefore, the observed improvements in mechanical performance can be attributed to the presence of a defect-free microstructure, enhanced phase homogeneity, and the absence of the graphite phase, as indicated by the aforementioned microstructural studies.

The augmentation of Mo loading up to 12% resulted in a reduction in the LSS value, suggesting that there was no extra potential for Mo loading concerning joint strength. The occurrence of fracture at the joint interface can be attributed to the separation of the Ni-Si and Ni-Mo-C-based layers by the precipitated graphite, as seen in Fig. 6.11h. This separation ultimately led to a significant decrease in the LSS value, which reached a level as low as 75 MPa. Therefore, the study concluded that the addition of 8% Mo in a Ni-30Si alloy is the optimal composition for achieving a high-strength SiC-SiC joint. This composition effectively mitigated thermal residual stresses and prevented the formation of any defects. The interface was found to exhibit the presence of newly produced phases, namely δ-Ni_2Si, Ni_3Si_2, Mo_2C, and Ni_3Mo_3C, in the absence of graphite. In summary, the pressure-less brazing procedure has successfully achieved a better SiC-SiC joint with high-temperature stable phases and exceptional shear strength, as evidenced by the literature reported in Table 6.2. The shear strength obtained in our study is comparable to the work reported by Li et al. employing Si-

24Ti-3CNT braze alloy (Li et al. 2020). It is important to note that their alloy is Si-rich, and while Si is known to provide great mechanical strength at room temperature, it is not suitable for high-temperature applications due to possible difficulties at the Si-SiC interface, where debonding can begin and propagate, resulting in joint failure (Singh et al. 1994, Yin et al. 2010).

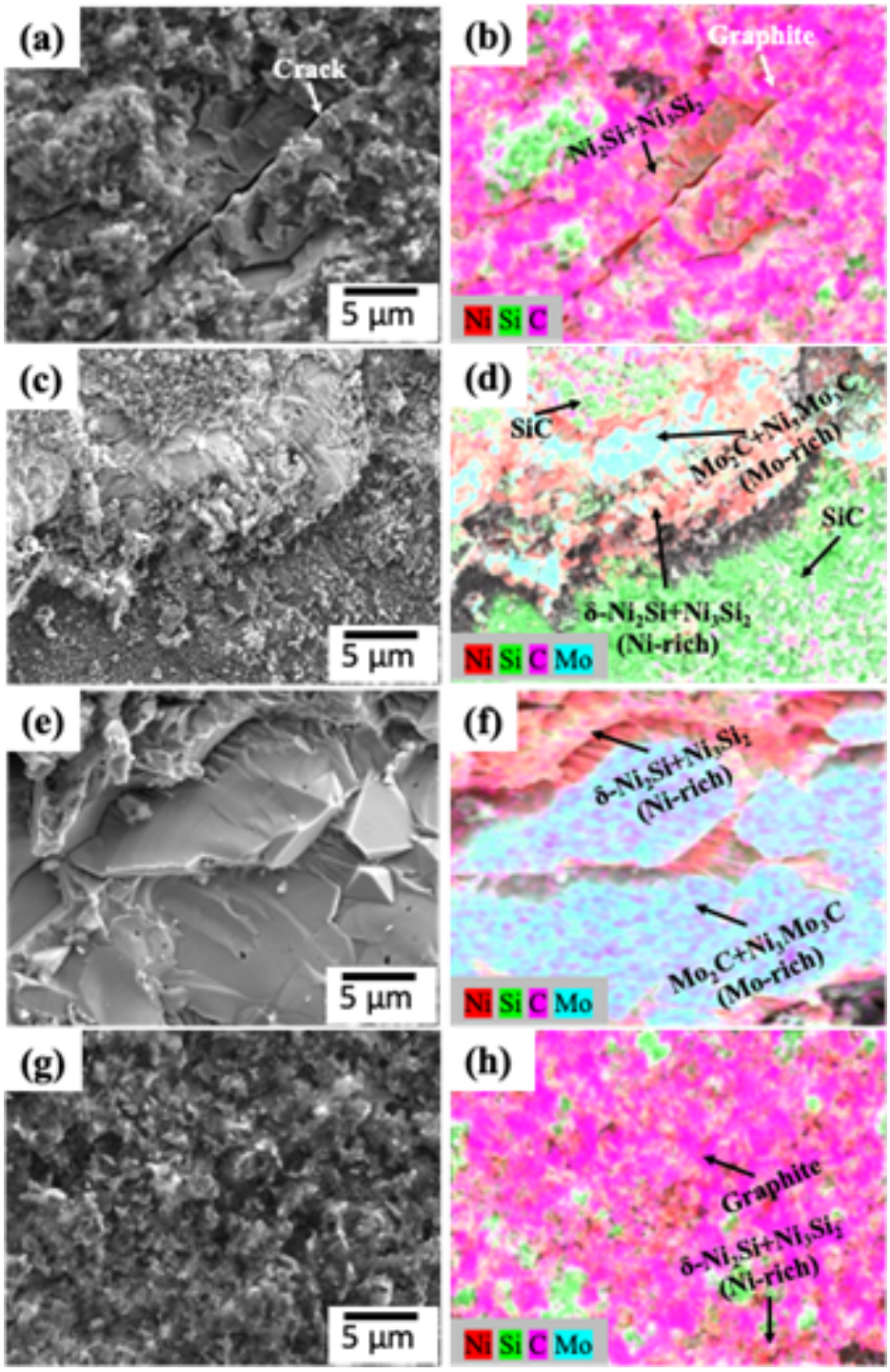

Fig. 6.11: SEM-EDS analysis for fracture surface of (a, b) J-Mo-0; (c, d) J-Mo-4; (e, f) J-Mo-8; and (g, h) J-Mo-12.

Table 6.2: Literature reported shear strength of α-SiC ceramic joints by brazing process

Filler	Parameters	LSS (MPa)	Remarks	Ref.
Si-24Ti-3CNTs	1380ºC, 20 min	108.1	Si-rich, CNTs agglomeration, HT[#]	Li 2020
Si-Cr-Y	1380ºC, 20 min,	88.1	Si-rich, HT[#], LS[$]	Li 2018
Si-Ti	1500ºC, 60 min	76.2	HT, LS	Ma 2020
Ti-Si-FeCoNi	1500ºC, 60 min	73.7	HT, LS	Wu 2022
CoFeCrNiCu	1180ºC, 60 min	60	LS	Wang 2020
Zr-Cu	1200ºC, 20 min	57	LS	Zhou 2020
AgCuTi+GNP	900ºC, 10 min	38	LS, LST[$$]	Song 2019a
Sn-Ti	950ºC, 10 min,	32	LS, LST[$$]	Fu 2020
Ni	1245ºC, 60 min	29.4	LS	Shi 2020
Ni-Si-Mo	1300ºC, 30 min	107	High LSS	This work
[$]: LS:Low strength, [#]: HT: High temperature, [$$]:LST: Low service temperature				

6.3.4 Joining mechanism

The aforementioned findings have led to the development of a theoretical framework for the joining of α-SiC using different Mo-modified Ni-30Si fillers. The complete process can be categorised into the following stages: (i) brazing stage, (ii) bonding stage, and (iii) testing stage (Fig. 6.12).

In the case of the J-Mo-0 joint (Fig. 6.12a), the filler material undergoes melting as a result of the eutectic composition, leading to rapid wetting of the SiC surface. Ni tends to diffuse towards the substrate side, whereas Si and C from SiC undergo counter-diffusion towards the filler. Ni demonstrates a notable affinity towards SiC, resulting in its reaction and subsequent formation of δ-Ni_2Si and Ni_3Si_2. This reaction is accompanied by the release of graphite atoms. Graphite has limited solubility in Ni-Si-based compounds, leading to its precipitation as a separate phase at the IRZ. In addition, it should be noted that at ~1300ºC, a portion of the liquid filler undergoes a conversion into θ-Ni_2Si, as indicated by the reaction (6.8). Subsequently, during the cooling process, this θ-Ni_2Si compound further undergoes a peritectic transformation by interaction with the remaining liquid fraction, as described by reaction (6.9), resulting in the formation of δ-Ni_2Si.

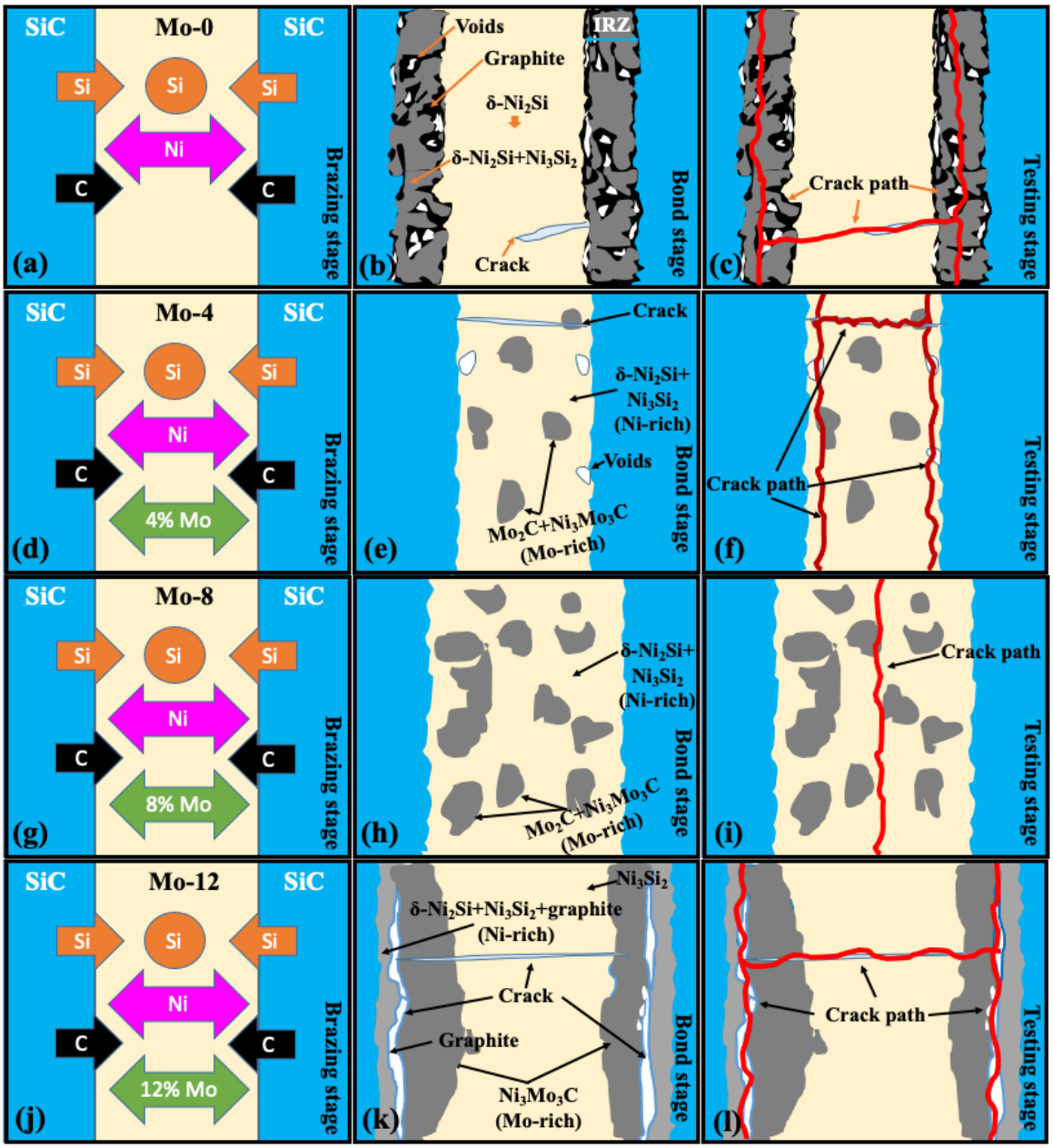

Fig. 6.12: Conceptual interfacial microstructural evolution model: (a)-(c) J-Mo-0, (d)-(f) J-Mo-4, (g)-(i) J-Mo-8, and (j)-(l) J-Mo-12 joints.

Based on the thermodynamic calculations presented in Fig. 6.5a and 6.5b, it is obvious that the liquid alloy δ-Ni_2Si and θ-Ni_2Si are in equilibrium with the graphite phase. Additionally, the partially liquid phase (θ-Ni_2Si) being unstable at low temperatures undergoes a eutectoid transformation below 825ºC throughout the cooling process, resulting in the formation of δ-Ni_2Si and Ni_3Si_2, as described by reaction (6.10). The nucleation of these phases begins at the surface of graphite, which acts as a heterogeneous nucleation site due to the large difference in their melting points. Thus, the aforementioned factors led to the emergence of Ni-

rich islands within the graphite clusters located in the IRZ. A fraction of the element Ni that remains at the central region of the interface undergoes a chemical reaction with Si, leading to the creation of δ-Ni_2Si. The production of δ-Ni_2Si and Ni_3Si_2 is thermodynamically feasible in comparison to other Ni-Si-based compounds as indicated by their lowest standard Gibbs free energy values (Kaufman et al. 1979). The thermodynamics calculations as depicted in Fig. 6.5, suggest that equilibriums are established among all the phases including δ-Ni_2Si, Ni_3Si_2, graphite, and SiC at the interface. The Gibbs free energy (ΔG) of all products is computed and illustrated in Fig. 6.13. The thermodynamic feasibility of the reaction between Ni and SiC, resulting in the synthesis of δ-Ni_2Si and Ni_3Si_2, is supported by the negative values of ΔG associated with reactions (6.1)-(6.5). Due to a significant disparity in the CTE between the filler (13.6×10^{-6}/°C) and SiC (3×10^{-6}/°C), the interphase (~43 μm in thickness) experienced high thermal stresses. Consequently, defects are generated at the joining regions, as depicted in Fig. 6.12b. When an external load is applied, these defects, together with graphite phases within the joint, are especially prone to fracture initiation and propagation along the interlayer, eventually leading to bond failure as shown by the red line in Fig. 6.12c. The J-Mo-0 joint exhibited an undesirable adhesive mode failure, which can be attributed to the insufficient bonding between the filler and the substrate due to the presence of graphite and defects, as confirmed by fractography analysis (Fig. 6.11a and 6.11b).

$$Liquid \rightarrow \theta - Ni_2Si \tag{6.8}$$

$$Liquid + \theta - Ni_2Si \rightarrow \delta - Ni_2Si \tag{6.9}$$

$$\theta - Ni_2Si \rightarrow \delta - Ni_2Si + Ni_3Si_2 \tag{6.10}$$

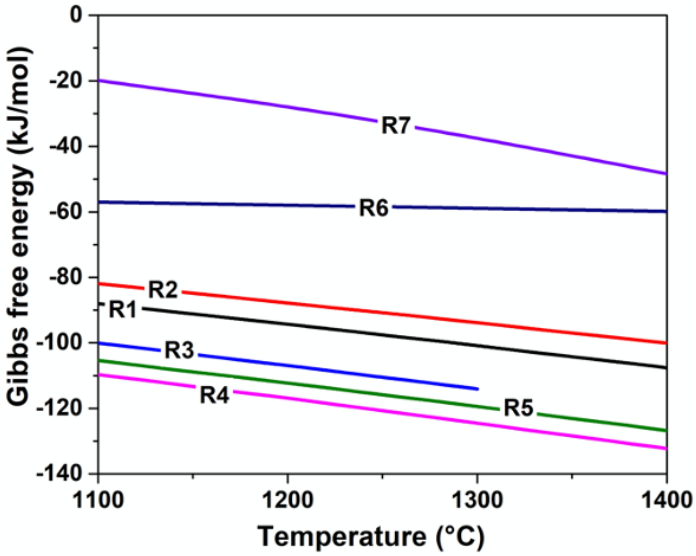

Fig. 6.13: Gibbs free energy (ΔG) of possible reactions.

Fig. 6.12d illustrates the joint that has been produced using a 4% Mo (J-Mo-4). In a manner akin to J-Mo-0, a part of Ni is consumed by the Si present in filler resulting in the formation of δ-Ni_2Si and Ni_3Si_2 phases, commonly referred to as the Ni-rich phase. This phase remained concentrated in the central region of the interface. Concurrently, the unreacted elements Ni and Mo exhibited diffusion towards the interface between the filler and SiC. Notably, the diffusion of Ni is faster than Mo owing to the high reactivity of the former towards SiC. Consequently, a reaction took place between Ni and SiC, resulting in the formation of δ-Ni_2Si and Ni_3Si_2 compounds. Additionally, this reaction led to the precipitation of graphite particles as a secondary product. The reaction between Mo in contact with graphite results in the formation of Mo_2C. Furthermore, a fraction of the Mo_2C compound undergoes a reaction with the pre-existing Ni, resulting in the formation of Ni_3Mo_3C. These newly formed structures, referred to as Mo-rich phases, are visually recognisable and are depicted in Fig. 6.12e. The Mo-rich phases are uniformly dispersed in the Ni-rich interphase matrix. The negative values of ΔG for Mo_2C (R6: -58 kJ/mol) and Ni_3Mo_3C (R7: -38 kJ/mol), as illustrated in Fig. 6.13, indicate that the formation of these compounds is expected to proceed spontaneously at 1300ºC. The Mo_2C phase, which is stable at room temperature is formed through a solid-state reaction, as depicted in Fig. 6.7a. This reaction occurs below the critical temperature (T_c: 1350ºC) following the reaction (Epicier et al. 1988, Groschner et al. 1994). As seen in the Ni-Mo-C phase diagram (Fig. 6.7b), the invariant peritectic reactions of liquid and Mo_2C as per reaction (6.12)-(6.14) are responsible for the formation of Ni_3Mo_3C.

$$Liquid \rightarrow Ni + Mo_2C + C \tag{6.11}$$

$$Liquid + Mo_2C \rightarrow Ni + Ni_3Mo_3C \tag{6.12}$$

$$Liquid + Mo_2C \rightarrow Ni_3Mo_3C + MoNi \tag{6.13}$$

$$Liquid + Mo_2C \rightarrow Ni_3Mo_3C \tag{6.14}$$

The inclusion of 4% Mo in the Ni-30Si alloy resulted in a decrease in the CTE to 6×10^{-6}/°C. This reduction played a significant role in mitigating residual thermal stresses at the joining interface during the cooling phase. Consequently, a narrower interface of ~26 μm (Fig. 6.12e) was achieved with a reduction in defects, which consequently improved the consolidation of the interlayer. During the LSS testing, it was seen that the initiation of fractures occurred in the interphase and then progressed across the void and pre-existing crack, resulting in joint failure (red line in Fig. 6.12f) in the proximity of SiC substrate, as observed in Fig.

6.11c and 6.11d. The introduction of a 4% Mo content in the J-Mo-4 filler resulted in a significant enhancement of the joint strength, increasing it from 36 MPa to 72 MPa. The observed mode of failure persisted as the unfavourable adhesive mode, suggesting that the capacity of the filler as a brazing material is not fully harnessed. The existence of a small amount of residual defects and graphite phase suggests that the loading of 4% Mo is inadequate in attaining a complete defects-free joint. Therefore, the Mo loading was increased to 8% to achieve a defects-free joint (J-Mo-8). In a manner akin to J-Mo-4, the elements Ni and Mo exhibited diffusion towards the SiC, while Si and C experienced diffusion towards the interphase (as illustrated in Fig. 6.12g). In this particular case, the interphase exhibited a thickening of ~ 40 μm and is characterised by two unique regions, specifically, a Ni-rich region and a Mo-rich region, as depicted in Fig. 6.12h. The Ni-rich zone is predominantly composed of δ-Ni_2Si and Ni_3Si_2 compounds, whereas the Mo-rich portion is dominated by Mo_2C with a tiny amount of Ni_3Mo_3C. Regarding the J-Mo-4 joint, the Mo-rich region experienced a threefold increase in size as a result of the Mo loading being doubled. Nevertheless, it remained uniformly distributed inside the Ni-rich zone. Consequently, the hetero-interfaces exhibited strong bonding with both the SiC and the filler, resulting in a flawlessly integrated joint devoid of any surface imperfections. Additionally, the presence of a higher concentration of Mo with an even distribution in the interphase resulted in a further reduction of the CTE to a value below 5.4×10^{-6}/°C. This drop in CTE helped to alleviate thermal stresses that occur during the cooling process, ultimately leading to the formation of a defect-free SiC joint. The cracks shown by the red line in Fig. 6.12i propagated through the filler material during the LSS test, correlating with fracture surface images (Fig. 6.11e and 6.11f). The absence of voids or excessive graphite content resulted in the interlayer effectively resisting the applied shear forces. As a result, a cohesive mode of failure occurred within the interlayer itself, demonstrating the complete utilisation of the brazing potential of the filler. The joint displayed a maximum LSS of 107 MPa, indicating that the bond interface possessed superior strength compared to the joints without Mo-content.

To conduct a more comprehensive analysis of the extent of Mo addition in Ni-30Si alloy, the Mo content is increased to 12% (Fig. 6.12j). The microstructural analysis reveals that excess loading of Mo drastically modifies the morphology of the joint. At the onset, Ni undergoes diffusion towards SiC, resulting in the formation of δ-Ni_2Si and Ni_3Si_2, accompanied by the liberation of carbon atoms. The deposition of δ-Ni_2Si and Ni_3Si_2 phases occurs in the form of a Ni-rich layered structure at the interface. The high affinity of the carbon atom for Mo causes it to migrate to the interlayer area, where it then transforms into Mo_2C. Additionally,

Mo_2C reacts with the locally available Ni to give rise to the formation of Ni_3Mo_3C phases. The presence of an ample quantity of Mo at the interface leads to an acceleration in the formation of Mo-rich phases. Consequently, the Mo_2C/Ni_3Mo_3C grains undergo coarsening and merge with neighbouring grains over the dwell period, resulting in the formation of a vertically continuous Mo-rich layer. As a result, there is a fifteen-fold increase in the area occupied by Mo-rich phases concerning the J-Mo-4. The graphite released during the reaction of Ni and SiC acts as the nucleation sites for both Ni and Mo-rich liquid braze (Shi et al. 2020, Shi et al. 2021a). Consequently, a thin layer of graphite is sandwiched between the Ni and Mo-rich phases. During the cooling process, the Ni-rich, Mo-rich, and graphite phases served as stress concentration sites due to notable variations in density, conductivity, and CTE. This resulted in the formation of cracks, as illustrated in Fig. 6.12k. The primary constituent of the filler is mostly Ni_3Si_2. This is primarily attributed to the fact that a substantial portion of the Ni is consumed by the presence of Mo-rich compounds, and the synthesis of δ-Ni_2Si requires a greater availability of Ni. The region with a high concentration of Mo in this particular scenario is primarily composed of Ni_3Mo_3C, which is formed through the reaction outlined in equations (6.11) to (6.14). It is noteworthy that the interphase thickness exhibited a significant increase of more than two-fold, reaching ~93 μm, in comparison to other Mo-based joints. This can be explained by the increase in unit cell volume of the newly formed phases. The volume expansion of the braze is calculated considering the crystal structure as suggested by XRD analysis. The details of the phases with corresponding crystal structure and unit cell volume are listed in Table 6.3.

Table 6.3: Crystal structure parameters and unit cell volume of various phases.

Compound	**Structure**	**JCPDS File No.**	**Lattice parameters (Å)**			**Volume ($Å^3$)**
			a	**b**	**c**	
δ-Ni_2Si	Orthorhombic	00-048-1339	7.0664	5.0088	3.7321	132.0946
Ni_3Si_2	Orthorhombic	04-023-6058	12.2174	10.8014	6.9222	913.4883
Mo_2C	Orthorhombic	04-003-0962	4.7240	6.0040	5.1990	147.4587
Ni_3Mo_3C	Cubic	04-005-4042	11.1400	11.1400	11.1400	1382.47

As discussed earlier, the joining interface of J-Mo-12 is predominantly composed of Ni_3Si_2 and Ni_3Mo_3C phases. During the cooling process, the θ-Ni_2Si phase transforms to Ni_3Si_2, resulting in a significant volumetric expansion of 590%. Furthermore, the increased formation

of Ni_3Mo_3C resulted in a substantial expansion of the unit cell volume, exhibiting a remarkable increase of 835%. Therefore, the excessive rise in interphase thickness seen in the case of J-Mo-12 can be attributed to the higher yields of Ni_3Si_2 and Ni_3Mo_3C phases. During the evaluation of LSS, the cracks propagated through the voids and graphite layer, confirmed by fractography images (Fig. 6.11g and 6.11h), are illustrated by the red line in Fig. 6.12l. The strength of the C-C bond in graphite is significantly lower between basal planes (7 kJ/mol) compared to within the planes (524 kJ/mol) due to its anisotropic sp^2 hybridization (Valenzuela et al. 2018). Consequently, under the influence of applied stress, the basal planes undergo facile debonding, serving as the primary locations for crack initiation. This process is subsequently expedited by interactions with voids (Shi et al. 2021a). Furthermore, the considerable thickness of the interlayer, characterised by its brittleness, facilitated the rapid spread of cracks, ultimately failing the joint, as evidenced by the low LSS value of 75 MPa. In the end, the addition of an 8% Mo addition in a Ni-30Si alloy resulted in the formation of a defects-free joint. In this particular instance, the interphase consisted of uniformly dispersed high-temperature phases, namely Ni-based (δ-Ni_2Si+Ni_3Si_2) and Mo-based (Mo_2C+Ni_3Mo_3C) phases.

6.4 Conclusions

SiC ceramic was joined using Ni-30Si filler, incorporating varying concentrations of Mo (up to 12 at.%) at 1300 °C. This approach is employed to prevent the undesired residue of graphite within the joint. When the loading of Mo reached 8 %, the liquid alloy attained a state of thermodynamic equilibrium with SiC, and no graphite was observed at the interface. The goal of the present work was to evaluate the interfacial response mechanism and mechanical characteristics of the joint, both before and after the introduction of Mo. The Ni-30Si filler material exhibited limited suitability for brazing applications owing to its inadequate wettability characteristics, high residual stresses and suboptimal bonding properties of the reaction products, particularly graphite. The existence of graphite, which creates numerous cracks within the reaction zone, significantly compromises the integrity of the brazed joint. The introduction of Mo into the Ni-30Si alloy system resulted in the sequential occurrence of the Ni-Si and Ni-Mo-C reactions throughout the brazing process. When 8% Mo was loaded, a homogenous grain boundary without any graphite was observed. This grain boundary was successful in distributing the applied stress and preventing crack development, leading to an LSS of 107 MPa. The enhanced mechanical properties can be ascribed to the alterations in the

microstructure of the grain, transitioning from graphite-rich to high-temperature stable Ni-based (e.g., δ-Ni_2Si, Ni_3Si_2) and Mo-based (e.g., Mo_2C, Ni_3Mo_3C) phases. The experimental findings demonstrate a strong concurrence with the theoretical calculations, thereby substantiating the pivotal role of Mo content in influencing the reaction mechanism. When the Mo loading exceeds 12%, the reaction products demonstrate a significant increase in unit cell volume, leading to the development of a thicker interphase and a non-homogeneous distribution of the phases causing an increase in the concentration of residual graphite in the joint. Moreover, this phenomenon gives rise to the formation of an interfacial reaction region, hence resulting in a reduction in the strength of the joint. Consequently, the incorporation of 8% Mo into a Ni-30Si alloy yielded a SiC joint of superior quality, characterised by the presence of newly formed high-temperature stable phases (Ni-based and Mo-based) with even distribution, close to the contact region.

References:

(1) A. Kamal, A.K. Shukla, V.M. Shinde, B.V. Rajasekhar, Microstructure and mechanical properties of C/SiC-niobium alloy (C103) joint brazed with TiCuAg alloy for aerospace applications, Ceram. Int. 49 (2023) 29265-29273. https://doi.org/10.1016/j.ceramint.2023.06.218.

(2) A. Kamal, A.K. Shukla, V.M. Shinde, High-strength C/SiC joints prepared using a novel Ni-Si-CNTs-based filler, J. Eur. Ceram. Soc. 43 (2023) 7411-7421. https://doi.org/10.1016/j.jeurceramsoc.2023.08.024.

(3) B. Zhou, J. Wang, K. Feng, Y. Cai, S. Chen, Effect of Brazing Parameters on the Microstructure and Properties of SiC Ceramic Joint with Zr-Cu Filler Metal, Crystals 10 (2020) 93. https://doi.org/10.3390/cryst1002009.

(4) B.J. Kullen, N.M. Levitz, M.J. Steindler, Management of waste cladding hulls. Part II. An assessment of zirconium pyrophoricity and recommendations for handling waste hulls, United States N. P. (1977). https://doi.org/10.2172/5203818.

(5) C. Song, T. Lin, P. He, W. Yang, D. Jia, J. Feng, Microstructure evolution and its effect on the mechanical properties of the ZrC–SiC composite joint diffusion bonded with pure Ni foil, Ceram. Int. 40 (2014) 17-23. https://doi.org/10.1016/j.ceramint.2013.04.074.

(6) D. Chen, H. Gu, A. Huang, Y. Deng, Z. Shao, Incorporating Zr combined Si and C to achieve self-repairing ability and enhancement of silica sol bonded SiC castables, J. Alloys Compd. 732 (2018) 396-405. https://doi.org/10.1016/j.jallcom.2017.10.233.

(7) D. Sciti, A. Bellosi, L. Esposito, Bonding of zirconia to superalloy with the active brazing technique, J. Eur. Ceram. Soc. 21 (2001) 45–52. https://doi.org/10.1016/S0955-2219(00)00162-X.

(8) D. Vedela, O. Grigoriev, P. Mazur, A. Osipov, M. Brodnikovskyi, L. Silvestronib, Effect of Mo_2C addition on the mechanical properties and oxidation resistance of ZrB_2-SiC ceramics, J. Alloys Compd. 879 (2021) 160398. https://doi.org/10.1016/j.jallcom.2021.160398.

(9) E. Kurimoto, H. Harima, T. Toda, M. Sawada, M. Iwami, S. Nakashima, Raman study on the Ni/SiC interface reaction, J. Appl. Phys. 91 (2002) 10215. https://doi.org/10.1063/1.1473226.

(10) F. Moszner, G. Mata-Osoro, M. Chiodi, J. Janczak-Rusch, G. Blugan, J. Kuebler, Mechanical behaviour of SiC joints brazed using an active Ag–Cu–In–Ti braze at

elevated temperatures. Int J Appl Ceram Technol 14 (2017) 703–711. https://doi.org/10.1111/ijac.12689.

(11) F.J. Guo, Y.F. Wang, M.S. Wang, Q. He, H. Ran, C.X. Huang, Y.T. Zhu, Hetero-deformation induced strengthening and toughening of pure iron with inverse and multi-gradient structures, Mater. Sci. Eng. A. 782 (2020) 139256. https://doi.org/10.1016/j.msea.2020.139256.

(12) G. Wang, Y. Yang, R. He, C. Tan, M. Huttula, W. Cao, A novel high entropy CoFeCrNiCu alloy filler to braze SiC ceramics, J. Eur. Ceram. Soc. 40 (2020) 3391–3398. https://doi.org/10.1016/j.jeurceramsoc.2020.03.044.

(13) H. Long, S. Mao, Y. Liu, Z. Zhang, X. Han, Microstructural and compositional design of Ni-based single crystalline superalloys - A review, J. Alloys Compd. 743 (2018) 203-220. https://doi.org/10.1016/j.jallcom.2018.01.224.

(14) H. Shi, H. Peng, J. Yan, R., N. Li, Y. Wen, D. Bai, Z. Liu, Y. Chai, R. Zhang, M. Li, K. Chen, M. Luo, Q. Sun, R. Li, X. Dong, Investigations of the effect of Si addition on graphite elimination and the oxidation behaviour of SiC joint using Inconel 625 powder filler, J. Eur. Ceram. Soc. 42 (2022) 1258–1271. https://doi.org/10.1016/j.jeurceramsoc.2021.11.055.

(15) H. Shi, H. Peng, Y. Chai, N. Li, Y. Wen, D. Bai, Z. Liu, J. Yan, R. Zhang, M. Li, K. Chen, M. Luo, Q. Sun, R. Li, X. Dong, Effect of Zr addition on the interfacial reaction of the SiC joint brazed by Inconel 625 powder filler, J. Eur. Ceram. Soc. 41 (2021) 6238-6247.

(16) H. Shi, Y. Chai, N. Li, J. Yan, H. Peng, R. Zhang, M. Li, D. Bai, K. Chen, Z. Liu, M. Luo, Q. Sun, X. Zhu, Y. Zhang, R. Li, B. Zhang, X. Dong, Investigation of interfacial reaction mechanism between SiC and Inconel 625 superalloy using thermodynamic calculation, J. Eur. Ceram. Soc. 41 (2021) 3960–3969. https://doi.org/10.1016/j.jeurceramsoc.2021.02.046.

(17) H. Shi, Y. Chai, N. Li, J. Yan, X. Zhu, K. Chen, D. Bai, Z. Liu, M. Wu, R. Zhang, M. Li, M. Luo, Q. Sun, C. Xin, W. Hu, X. Dong, Interfacial reaction mechanism of SiC joints joined by pure nickel foil, J. Eur. Ceram. Soc. 40 (2020) 5162-5171. https://doi.org/10.1016/j.jeurceramsoc.2020.07.048.

(18) H.B. Ma, J.X. Xue, J.H. Zhai, T. Liu, Q.S. Ren, Y.H. Liao, L.X. Wu, W.M. Guo, S.K. Sun, H.T. Lin, Pressureless joining of silicon carbide using Ti_3SiC_2 MAX phase at 1500ºC, Ceram. Int. 46 (2020) 14269–14272. https://doi.org/10.1016/j.ceramint.2020.02.155.

(19) H.X. Li, Z.Q. Wang, Z.H. Zhong, Q. Wen, K.J. Song, H.B. Zhang, Y.C. Wu, Micro-alloying effects of yttrium on the microstructure and strength of silicon carbide joint brazed with chromium-silicon eutectic alloy, J. Alloys Compd. 738 (2018) 354-362. https://doi.org/10.1016/j.jallcom.2017.12.137.

(20) J.C. Feng, H.J. Liu, M. Naka, J.C. Schester, Reaction products and growth kinetics during diffusion bonding of SiC ceramic to Ni–Cr alloy, Mater Sci Technol 19 (2003) 137–142. https://doi.org/10.1179/174328413X13789825316707.

(21) J.G. Valenzuela, A. Bertarelli, F. Carra, N. Mariani, S. Bizzaro, R. Arenal, Development and properties of high thermal conductivity molybdenum carbide - graphite composites, Carbon 135 (2018) 72-84. https://doi.org/10.1016/j.carbon.2018.04.010.

(22) L. Kaufman, Coupled phase diagrams and thermochemical data for transition metal binary systems-VI, CALPHAD 3 (1979) 45-76. https://doi.org/10.1016/0364-5916(79)90020-8.

(23) L. Zhang, K.N. Tu, Structure and properties of lead-free solders bearing micro and nanoparticles, Mater. Sci. Eng. R Rep. 82 (2014) 1-32, http://dx.doi.org/10.1016/j.mser.2014.06.001.

(24) L.L. Snead, T. Nozawa, Y. Katoh, T.S. Byun, S. Kondo, D.A. Petti, Handbook of SiC properties for fuel performance modelling, J. Nucl. Mater. 371 (2007) 329–377, https://doi.org/10.1016/j.jnucmat.2007.05.016.

(25) L.X. Wu, J.X. Xue, J.H. Zhai, H.B. Ma, Y. Liu, Q.S. Ren, Y.H. Liao, S.K. Sun, W.M. Guo, L.L. Zhu, H.T. Lin, The improved SiC joints prepared by pressureless braze joining using Ti–Si interlayer with metallic infiltration, Ceram. Int. 48 (2022) 37049–37054. https://doi.org/10.1016/j.ceramint.2022.08.279.

(26) M. Groschner, P. Ettmayer, W. Lengauer, and H. Kolaska, The melting behaviour of Ni-Mo-C and Co-Mo-C alloys, Rev. Metall. 91(1994) 1767-1775. https://doi.org/10.1051/metal/199491121767.

(27) M. Liu, J. Zheng, Y. Lu, Z. Li, Y. Zou, X. Yu, X. Zhou, Investigation on corrosion behaviour of Ni-based alloys in molten fluoride salt using synchrotron radiation techniques, J. Nucl. Mater. 440 (2013) 124-128. https://doi.org/10.1016/j.jnucmat.2013.04.056.

(28) M. Singh, D.R. Behrendt, Reactive melt infiltration of silicon-niobium alloys in microporous carbons, J. Mater. Res. 9 (1994) 1701–1708. https://doi.org/10.1557/JMR.1994.1701.

(29) M. Xu, H. Liu, H. Zhao, W. Li, How to Decrease the Viscosity of Suspension with the Second Fluid and Nanoparticles?, Sci. Rep. 3 (2013) 3137. https://doi.org/10.1038/srep03137.

(30) P. Tao, Y. Wang, Fabrication of highly dense three-layer SiC cladding tube by chemical vapour infiltration method, J. Am. Ceram. Soc. 102 (2019) 6939–6945, https://doi.org/10.1111/jace.16552.

(31) P. Tatarko, V. Casalegno, C. Hu, M. Salvo, M. Ferraris, M.J. Reece, Joining of CVD-SiC coated and uncoated fibre reinforced ceramic matrix composites with pre-sintered Ti_3SiC_2 MAX phase using Spark Plasma Sintering, J. Eur. Ceram. Soc. 36 (2016) 3957-3967. https://doi.org/doi:10.1016/j.jeurceramsoc.2016.06.025.

(32) S.G.K. Manikandan, D. Sivakumar, M. Kamaraj, Welding the Inconel 718 Superalloy: Reduction of Micro-segregation and Laves Phases, Elsevier (2019). https://doi.org/10.1016/C2018-0-01653-9.

(33) T. Epicier, J. Dubois, C. Esnouf, G. Fantozzi, P. Convert, Neutron powder diffraction studies of transition metal hemicarbides M_2C_{1-x}-II. In situ high-temperature study on W_2C_{1-x} and Mo_2C_{1-x}, Acta Metall. 36 (1988) 1903-1921. https://doi.org/10.1016/0001-6160(88)90293-3.

(34) W. Fu, X. Song, R. Tian, Y. Lei, W. Long, S. Zhong, J. Fenga, Wettability and joining of SiC by Sn-Ti: Microstructure and mechanical properties, J. Mater. Sci. Technol. 40 (2020) 15–23. https://doi.org/10.1016/j.jmst.2019.08.040.

(35) W.B. Tian, Z.M. Sun, P. Zhang, Y.M. Zhang, J. Shi, Brazing of silicon carbide ceramics with Ni-Si-Ti powder mixtures, J. Aust. Ceram. Soc. 53 (2017) 511–516. https://doi.org/10.1007/s41779-017-0061-7.

(36) X. Hernandez, C. Jiménez, K. Mergia, P. Yialouris, S. Messoloras, V. Liedtke, C. Wilhelmi, J. Barcena, An innovative joint structure for brazing C_f/SiC composite to titanium alloy, Mater. Eng. Perform. 23 (2014) 3069-3076. https://doi.org/10.1007/s11665-014-1074-9.

(37) X. Yin, S. He, L. Zhang, S. Fan, L. Cheng, G. Tian, T. Li, Fabrication and characterization of a carbon fibre-reinforced carbon–silicon carbide-titanium silicon carbide hybrid matrix composite, Mater. Sci. Eng. A 527 (2010) 835-841. https://doi.org/10.1016/j.msea.2009.08.069.

(38) Y. Cao, L. Nyborg, D.Q. Yi, U. Jelvestam, Study of reaction process on Ni/4H-SiC contact, Mater. Sci. Technol. 22 (2006) 1227–1234. https://doi.org/10.1179/174328406X118276.

(39) Y. Katoh, K. Ozawa, C. Shih, T. Nozawa, R. J. Shinavski, A. Hasegawa, L. L. Snead, Continuous SiC fibre, CVI SiC matrix composites for nuclear applications: Properties and irradiation effects, J. Nucl. Mater. 448 (2014) 448-476. http://dx.doi.org/10.1016/j.jnucmat.2013.06.040.

(40) Y. Liu, G. Wang,Y. Zhao, M. Wang, R. He, C. Tan, W. Wang, X. Zhou, Joining of SiC using CoFeCrNiCuTi high entropy alloy filler by electric current field assisted sintering, J. Eur. Ceram. Soc. 42 (2022) 1995-2003. https://doi.org/10.1016/j.jeurceramsoc.2021.12.063.

(41) Y. Liu, Y. Zhu, Y. Yang, X. Liu, Z. Huang, Microstructure of reaction layer and its effect on the joining strength of SiC/SiC joints brazed using Ag–Cu–In–Ti alloy. J Adv Ceram 3 (2014) 71–75. https://doi.org/10.1007/s40145-014-0095-z.

(42) Y. Liu, Z. R. Huang, X. J. Liu, Joining of sintered silicon carbide using ternary Ag–Cu–Ti active brazing alloy, Ceram. Int. 35 (2009) 3479–3484. https://doi.org/10.1016/j.ceramint.2009.03.016.

(43) Y. Song, D. Liu, S. Hu, X. Song, J. Cao, Graphene nanoplatelets reinforced AgCuTi composite filler for brazing SiC T ceramic, J. Eur. Ceram. Soc. 39 (2019) 696–704. https://doi.org/10.1016/j.jeurceramsoc.2018.11.046

(44) Y. Song, D. Liu, X. Song, S. Hu, J. Cao, In-situ synthesis of TiC nanoparticles during joining of SiC ceramic and GH99 superalloy, J. Am. Ceram. Soc. 102 (2019) 6529-6541. https://doi.org/10.1111/jace.16541.

(45) Y.N. Regmi, B.M. Leonard, General synthesis method for bimetallic carbides of group VIIIA first row transition metals with molybdenum and tungsten, Chem. Mater. 26 (8) (2014) 2609–2616. https://doi.org/10.1021/cm500076v.

(46) Z. Fathian, A. Maleki, B. Niroumand, Synthesis and characterization of ceramic nanoparticles reinforced lead-free solder, Ceram. Int. 43 (2017) 5302–5310, http://dx.doi.org/10.1016/j.ceramint.2017.01.067.

(47) Z. Li, R. Wei, Q. Wen, Z. Zhong, K. Song, Y. Wu, Microstructure and mechanical properties of SiC ceramic joints vacuum brazed with in-situ formed SiC particulate reinforced Si–24Ti alloy, Vacuum 173 (2020) 109160, https://doi.org/10.1016/j.vacuum.2019.109160.

(48) Z. Wang, Y. Liu, H. Zhang, J. Jiang, T. Lin, X. Liu, Z. Huang, Joining of SiC ceramics using the Ni-Mo filler alloy for heat exchanger applications, J. Eur. Ceram. Soc. 41 (2021) 7533-7542. https://doi.org/10.1016/j.jeurceramsoc.2021.07.056.